Precision Engineering 90 (2024) 108–121

Contents lists available at ScienceDirect

Precision Engineering

journal homepage: www.elsevier.com/locate/precision

PACS: Projection-driven with Adaptive CADs X-ray Scatter compensation for additive manufacturing inspection☆

Domenico Iuso *, Pavel Paramonov, Jan De Beenhouwer, Jan Sijbers

imec-Vision Lab, Department of Physics, University of Antwerp, Antwerp, 2610, Belgium
DynXlab: Center for 4D Quantitative X-ray Imaging and Analysis, Antwerp, 2610, Belgium

ARTICLE INFO

Keywords:
Additive manufacturing
X-ray scatter
Projection-based
Mesh
CAD
X-ray CT

ABSTRACT

Additive Manufacturing (AM) has revolutionised the production of custom-shaped samples through direct manufacturing from digital design models. As the internal structural integrity of these printed samples is of critical importance in diverse applications, X-ray radiography and X-ray Computer Tomography (X-CT) have emerged as widely used non-destructive imaging methods for quality control of AM samples. Unfortunately, beam hardening and X-ray scatter often degrade the quality of X-CT images, posing a significant challenge for X-ray based inspection.

In addressing X-ray scatter, most of the methodologies assume fixed scanning geometries or stationary/known object characteristics, limiting their practicality in dynamic industrial scenarios where these may change over time. Simulation-based methods have been proposed that estimate and suppress scatter by accurately simulating the forward projection process. Yet, these methods assume the availability of X-CT reconstruction for simulation, thereby requiring a large number of projections (and hence scan time) for faithful X-CT reconstruction.

In this work, we propose a simulation-based scatter compensation method (PACS) that eliminates the need for a prior X-CT scan. By employing few projections and nominal surface meshes of the scanned objects, the actual pose of the objects and their superficial deviation (e.g., due to printing) are estimated and used during X-ray simulations. Furthermore, as the pipeline is inherently coupled with a mesh projector, analysis of projective residuals facilitates the inspection for deformities or defects within the scanned object. To demonstrate the versatility of PACS for mitigating scatter, experiments across various inspection scenarios are conducted, and the outcomes are compared with those of a well-established scatter compensation technique. The results consistently show a higher Signal-to-Noise Ratio and Contrast-to-Noise Ratio of pore-defects, as well as lower residual errors in all examined cases.

1. Introduction

In recent years, Additive Manufacturing (AM), commonly referred to as 3D printing, has emerged as a manufacturing technique. Unlike traditional methods, AM allows for the construction of intricate structures layer by layer, guided by Computer-Aided Design (CAD) models, offering unmatched design flexibility. However, during printing, AM components are vulnerable to deformation and formation of defects such as keyholes and lack-of-fusion pores. To address these concerns, non-destructive imaging techniques like digital X-ray radiography and X-ray Computed Tomography (X-CT) are used for ensuring nominal printing parameters [1] or inspection of common defects down to the micrometer scale [2].

The ability to accurately identify defects relies on image quality, which can be significantly degraded by beam-hardening or scatter artefacts. Previous works have proposed both hardware- and software-based solutions to mitigate the impact of scattering. Hardware-based approaches seek to reduce scattered radiation by implementing measures such as adjusting detector positioning [3], using bow-tie filters [4], employing anti-scatter grids [5], or introducing beam-stop/beam-hole arrangements [6]. These strategies, however, require tailored modifications to scanning procedures, geometry, or radiation dosage, limiting their versatility. Conversely, software-based methods offer valuable alternatives. Scatter-deconvolution methods leverage the concept of an X-ray source composed of multiple pencil beams, each generating independent scattered radiation [7]. By characterising the

☆ This paper was recommended by Associate editor Dr. Masonori Kunieda.

* Corresponding author at: imec-Vision Lab, Department of Physics, University of Antwerp, Antwerp, 2610, Belgium.
E-mail address: Domenico.Iuso@uantwerpen.be (D. Iuso).

https://doi.org/10.1016/j.precisioneng.2024.08.006
Received 5 May 2024; Received in revised form 29 July 2024; Accepted 13 August 2024

scattered radiation from each beam based on known object composition, scatter-kernel parameters can be estimated. Subsequent deconvolution of the scattered radiation in the projection domain presents a computationally efficient solution. Different variations of this technique, accounting for factors such as asymmetry [8], attenuation-dependent kernels [9], accurate scatter models [10], and primary beam energy dependence [11], have been investigated. Deep learning approaches, often involving U-Net models, have also shown promise in scatter compensation. Lee and Lee demonstrated the efficacy of DL for image correction by training on simulated data, achieving significant scatter artefact reduction [12]. Griner et al. further advanced this by applying DL to suppress scatter artefacts in X-CT, enhancing image clarity and accuracy [13]. Nomura et al. took a novel approach by implementing DL for scatter compensation directly in the projection space, significantly improving image quality [14]. Additionally, Van der Heyden et al. combined DL with Monte Carlo simulations, demonstrating that DL can improve and complement the accuracy of these simulations in scatter removal [15]. However, the lack of explainable and trustworthy behaviour remains an issue. Recent endeavors have sought to enhance trust in deep learning models by introducing more transparent behaviour. Roser's method utilises splines to model and suppress the low-frequency components of scattered radiation, with parameters controlled by a neural network architecture [16]. Iskender's work involves a neural model simulating X-ray propagation and scattering across perpendicular planes along the optical axis, offering promising outcomes [17]. In contrast, heuristic techniques leverage prior knowledge of specific X-CT applications by utilising object symmetries [18] or approximating scattered radiation as blurred projections, specifically targeting cupping artefacts caused by scattered radiation [19]. Analytical X-ray scatter compensation methods are capable of modelling first-order scattered radiation in homogeneous or composite objects [20], which can be then subtracted from projections, where multiple scattering is sometimes simply modelled as a constant value across the detector pixels [21]. Simulation-based scatter compensation methods fall into two categories: those simulating X-ray propagation through voxelised volumes (Monte Carlo or deterministic) and those simulating propagation through surface meshes of scanned objects. Shiroma et al. developed a scatter correction method for industrial cone-beam CT (CBCT) using a fast GPU-based Linear Boltzmann Transport Equation (LBTE) solver called 3D VSHARP, which significantly reduces computational time while maintaining high accuracy in scatter correction [22]. Maslowski et al. introduced Acuros CTS, a fast solver for computed tomography scatter using the linear Boltzmann transport equation and validated for its core algorithms [23]. Xu et al. presented a fast cone-beam CT scatter correction method using GPU-based Monte Carlo simulation, enhancing the speed of scatter correction processes, making it suitable for real-time applications [24]. These methods necessitate a voxelised volume, usually obtained through a prior X-CT scan. Recently, methods tailored for AM have used the information contained in CAD models of the scanned object for X-ray scatter compensation. The feasibility of this approach was first proven by Xia et al. [25], and later Iuso et al. [26] implemented a mesh alignment procedure based on a prior X-CT scan for accurate X-CT scatter compensation. All these simulation methods can replicate the scanning scenario, simulating X-ray for each projection of the scan or, for faster estimation of scattered radiation, by simulating a minimal sub-group of projections or a coarsely-sampled volume.

All of the X-ray scatter compensation methods mentioned above require a training procedure, such as those employing scatter-kernels or deep learning, impose constraints on the object's shape, or assume the availability of a prior X-CT reconstruction. The requirement for a (computationally expensive and data demanding) prior X-CT reconstruction can be circumvented by employing a mesh projector (e.g., [27]). The mesh projector efficiently estimates the position and orientation of AM parts during scanning using only a few X-ray projections, so that an X-CT reconstruction of the object is not required. This means that simulation-based scatter compensation techniques can be finally applied in scenarios where obtaining an X-CT is not possible, for example in case only few projections are available. Moreover, the originally-designed surface-meshes can be deformed and adapted to the real printed sample, for an accurate X-ray scatter compensation of the scattered radiation by the printed part and any other object present in the scene (e.g., the physical supporting elements on which the sample is put during the scan). Finally, the use of the mesh projector eliminates the need to align meshes with different digital origins (often resulting in different sampling patterns): the CAD model created by the designer of the part and the surface-mesh extracted from the X-CT (e.g., generated by the marching cubes algorithm [28]).

In this study, an X-ray scatter compensation method (PACS) is presented that is based on efficient simulations of X-ray interactions using the CAD model of scanned AM objects. Unlike existing simulation-based approaches, this method does not require the availability of a prior CT reconstruction, where CAD models are matched to the scanned objects through just a few X-ray projections. PACS eliminates the need for deep learning training and geometry-dependent scatter libraries calculations. Additionally, to expedite simulations, we investigate strategies for downsizing the simulation problem. We demonstrate the effectiveness of our method across various scenarios, including poly-chromatic radiography-based analysis, discrete poly-chromatic X-CT reconstruction (based on DART [29]), and conventional poly-chromatic X-CT reconstructions, comparing its performance against an established scatter compensation method.

2. Materials

Scans were acquired with the FleXCT micro-CT scanning device, as detailed in [30]. The device was equipped with a 2880×2880 detector with pixels of size $150\,\mu m$. The scanned object was an AM component, specifically a bevel gear (as shown in Fig. 1), which was fabricated using a Form 3+ Low Force Stereolithography (LFS)^{TM} 3D printer by Formlabs, utilising Draft Resin (Formlabs).The choice of a plastic AM component was motivated by several factors: the need for a larger sample (compared to our previous study [26]) to enhance the amount of detected scattered radiation, which is more effectively achieved with a plastic part due to its size and the resulting smaller distance between the object and detector, and constraints in our micro-CT device that limit its capability to scan thicker metallic objects without introducing photon starvation artefacts. During the scan, the AM part was supported by 3D-printed components constructed from Polyamide 12. The source-to-detector distance was $800\,mm$ and the source-to-object distance was $320\,mm$. A tube voltage of $150\,kV_p$ was applied and the beam was filtered with $1.5\,mm$ aluminum.

The complete scan comprised 3000 projections, equiangularly distributed in the range [0°, 360°]. However, in the industrial quality inspection of AM samples, such a high number of projection images may not always be available. To accommodate this, three datasets were created, each corresponding to a distinct inspection scenario. The first dataset was designed for projection-based inspection and consisted of ten equiangularly sampled projections, and therefore labelled '10P'. The second dataset included 100 equiangularly sampled projections and was intended for X-CT inspection using discrete reconstruction of X-CT images, and therefore labelled '100P'. Lastly, the third dataset, designed for X-CT-based inspection through conventional CT reconstruction, encompassed the entire set of 3000 projection images, and is thus referred to as '3000P'. A discrete reconstruction applied to 100P was obtained through the poly-chromatic version of DART [29] (poly-DART), while conventional X-CT image reconstruction was achieved using poly-chromatic projective error minimisation based on Barzilai–Borwein optimisation [31], referred to as poly-BB. Both poly-DART and poly-BB were built on a distributed version of the ASTRA toolbox [32].

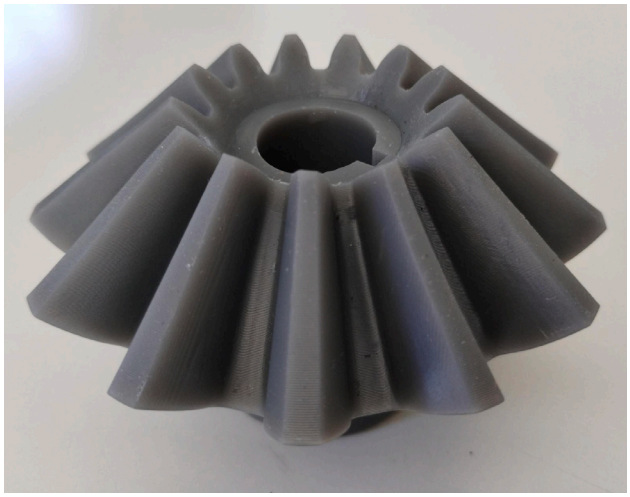

Fig. 1. A photo of the bevel gear.

3. Methods

The proposed scatter compensation pipeline relies on three essential operations: (1) estimating the object's pose and shape from few X-ray projections (Section 3.1), (2) predicting scatter for each individual X-ray projection (Section 3.2), and (3) compensating for scattered radiation in the actual X-ray projections (Section 3.3). The complete pipeline, inclusive of accessory information/operations, is graphically shown in Fig. 2.

3.1. Multi-object pose and shape estimation

Accurate scatter compensation in X-CT scans requires estimation of the pose of the scanned objects and possible deviations from their nominal shape (e.g., due to the printing process). To achieve this, we employ the nominal surface model of each object from its CAD model along with a mesh projector (CAD-ASTRA [27]) to iteratively estimate the object's position and orientation. This rigid pose estimation then serves as the starting point for iterative estimation of the (possibly deformed) object shape.

Let K denote the number of objects, where each object $k = 1, \dots, K$ is represented by its surface mesh denoted as $\boldsymbol{m}_k = (\boldsymbol{V}_k, \boldsymbol{N}_k)$. Here, $\boldsymbol{V}_k = \{\boldsymbol{v}_{ik}\} \in \mathbb{R}^{V\times 3}$ represents the V vertices of the mesh, and $\boldsymbol{N}_k = \{\boldsymbol{n}_{jk}\} \in \mathbb{R}^{N\times 3}$ the normals of its N triangular faces. During pose estimation, the mesh vertices $\boldsymbol{V}_k$ undergo a roto-translation described by a pose vector $\boldsymbol{\theta}_k \in \mathbb{R}^6$, consisting of three parameters for translation and three for orientation. The iterative refinement begins with an initial position and orientation assumption, where all objects are initially aligned along the vertical axis passing through the centre of rotation of the scan. Subsequently, the estimation process minimises the discrepancy between the measured projections $\boldsymbol{P} \in \mathbb{R}^M$ and the simulated projections, where M is the product of the number of projections and their number of pixels, leading to:

$$\tilde{\boldsymbol{\theta}}_1, \dots, \tilde{\boldsymbol{\theta}}_K = \arg\min_{\boldsymbol{\theta}_1,\dots,\boldsymbol{\theta}_K} \left\| \boldsymbol{P} - \sum_{k=1}^{K} \mathrm{PolyProj}_d \left[\mathrm{A}_{\boldsymbol{\theta}_k}[\boldsymbol{V}_k] \right] \right\|_2^2 . \tag{1}$$

Here, the $\mathrm{PolyProj}_d : \mathbb{R}^{V\times 3} \to \mathbb{R}^M$ operator simulates the polychromatic projections through the metadata d representing the vertices connectivity and material optical properties, while $\mathrm{A}_{\boldsymbol{\theta}_k} : \mathbb{R}^{V\times 3} \to \mathbb{R}^{V\times 3}$ represents a roto-translation operator that depends on the pose parameters $\boldsymbol{\theta}_k$.

Subsequently, registered meshes are employed for estimating the deformed shape of the AM samples. This deformation is described as per-vertex shifts from the nominal registered surface mesh of the CAD model. Similar to pose estimation, this involves iterative refinement of a linear programming problem. Besides a data consistency term, regularisation terms are introduced penalise significant changes in mesh topology. This linear programming problem is formulated as:

$$\tilde{\boldsymbol{V}}_1, \dots, \tilde{\boldsymbol{V}}_K = \arg\min_{\boldsymbol{\theta}_1,\dots,\boldsymbol{\theta}_K} \left\| \boldsymbol{P} - \sum_{k=1}^{K} \mathrm{PolyProj}_d \left[\mathrm{A}_{\tilde{\boldsymbol{\theta}}_k}[\boldsymbol{V}_k] \right] \right\|_2^2 + \sum_{k=1}^{K} \left(\alpha \left\| \boldsymbol{V}_k^* - \boldsymbol{V}_k \right\|_2^2 + \beta \left\| \boldsymbol{N}_k^* - \boldsymbol{N}_k \right\|_2^2 \right) . \tag{2}$$

Here, for each kth mesh, the distance between the vertices $\boldsymbol{V}_k$ and original vertices $\boldsymbol{V}_k^*$ is measured, where the difference $\boldsymbol{V}_k^* - \boldsymbol{V}_k$ symbolically represents the difference $\boldsymbol{v}_{ik}^* - \boldsymbol{v}_{ik}$ between each of the i vertices of the kth mesh. An analogous explanation applies to $\boldsymbol{N}_k^* - \boldsymbol{N}_k$ and $\boldsymbol{n}_{jk}^* - \boldsymbol{n}_{jk}$. These regularisation terms are governed by the parameters α and β during minimisation of the projection error of (2). Both the linear programming problems (1) and (2) are solved using the Adam optimiser.

3.2. X-ray interaction simulation

From the available simulation software [33–37], as well as specialised X-ray scatter simulation [23,38], the Monte Carlo (MC) photon transport simulator GATE [35] (version 9.2, built on Geant4 version 11.1.2) was chosen due to its widespread adoption and extensive validation in literature. Geant4 is a robust tool known for its accurate physical models across a variety of materials, making our method versatile and unbiased towards any specific material, whether metals or other substances. Information about the scanning system, such as scanning geometry and X-ray source operating parameters, was obtained from the experimental scan data and used for the GATE simulations. Additionally, the adapted surface meshes of all objects in the scan (as detailed in Section 3.1), were incorporated into the simulation. The simulation was configured to produce two outputs: the X-ray radiation detected by the detector, $\hat{\boldsymbol{P}}$, and the portion of $\hat{\boldsymbol{P}}$ that underwent at least one either Compton or Rayleigh scattering event within the object or its supporting elements. This portion is referred to as $\hat{\boldsymbol{S}}$. Since the FleXCT detector, along with the majority of industrial X-CT systems, is energy-integrating, the simulated detector is designed to compute the cumulative energy contribution of each incident photon. Each contribution is multiplied by the detector's sensitivity corresponding to the photon's energy.

In addition to $\hat{\boldsymbol{P}}$ and $\hat{\boldsymbol{S}}$, the white-field image $\hat{\boldsymbol{W}}$, which represents the unattenuated X-ray radiation, is obtained through an identical simulation without attenuating objects. To minimise the statistical MC fluctuations in the radiation detected by each pixel of the simulated white-field image, the simulated white-field image is fitted with an analytical function for point-wise radiative emission over a finite square detector element. The derivation of this analytical function for flat detectors is provided in Appendix A.

3.2.1. Accelerating MC simulations

X-ray physical interaction simulations conducted with GATE are known for their high accuracy, but also for slow execution times. To address this issue, our approach focuses on two main strategies: parallelisation of simulations and leveraging the physical behaviour of X-ray scattering. For the parallelisation of simulations, a software manager that is tailored for the GATE simulations has been developed, based on Message-Parsing Interface libraries (MPI). This manager is responsible for partitioning simulation tasks across CPU-clusters, running parallel instances across computing nodes, and merging the results. The MPI-manager is publicly accessible on GitHub [39], it is platform-independent in terms of workload management systems (e.g., Portable Batch System (PBS), Simple Linux Utility for Resource Management

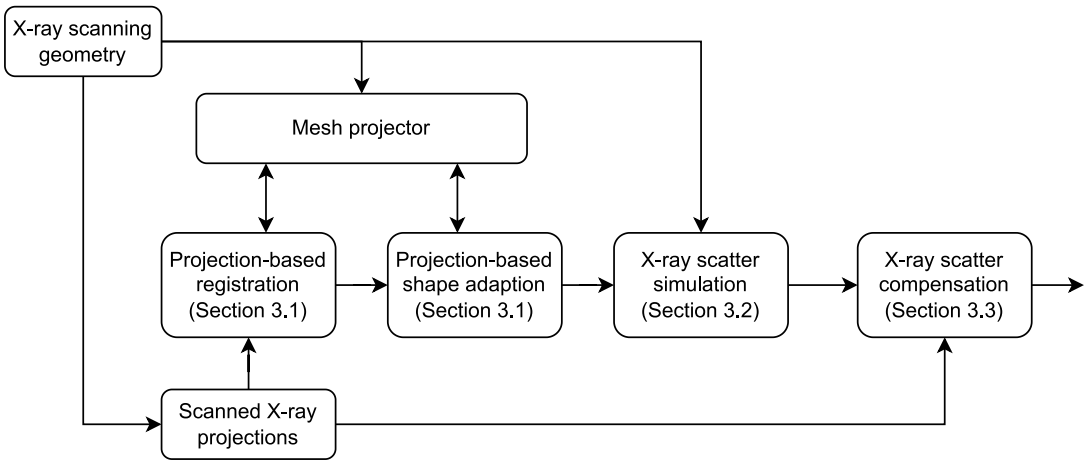

Fig. 2. A schematic of the scatter compensation pipeline of PACS. Once the user has chosen an appropriate X-ray scanning geometry for the objects to be scanned and X-ray projections are obtained, it is possible to estimate the pose of objects during the scan, and subsequently possible deviations from their CAD models. This information is mandatory for simulating the X-ray scattered radiation that was detected during the X-ray scan, which is later compensated in the scanned X-ray projections. To note that the X-ray scanning geometry is also an essential piece of information for the mesh projector and the X-ray scattering simulation.

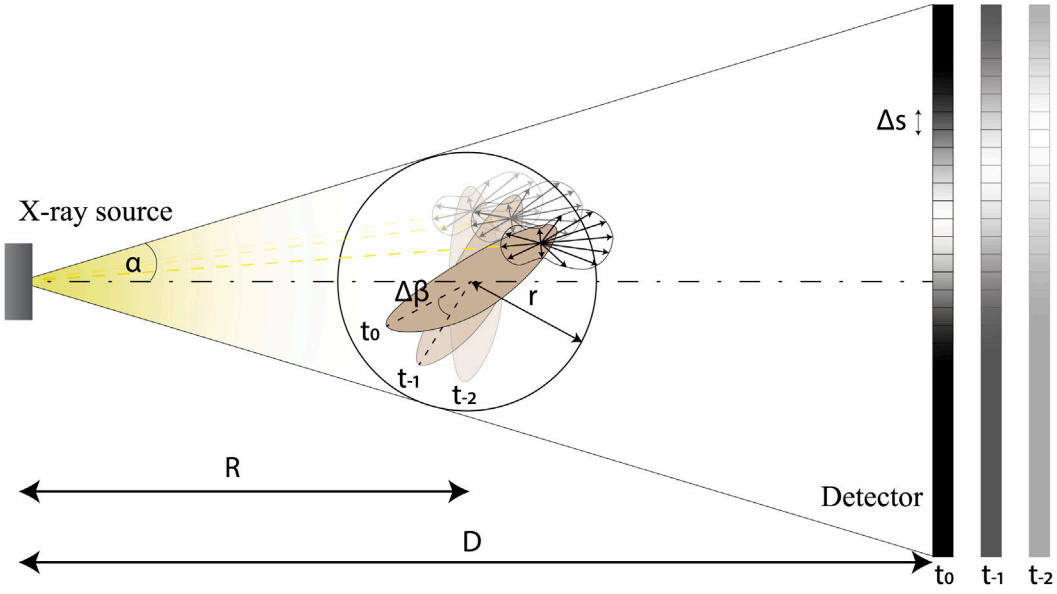

Fig. 3. Every minuscule region of the scanned object (brown) scatters X-ray radiation with a specific density per steradian. This figure illustrates the contribution of a scattering region of the object on the detector reading throughout three subsequent X-ray projections. Spatial frequencies of the scattered radiation are observed across the detector for a specific projection, while temporal frequencies are observed across subsequent projections for a specific detector pixel.

(SLURM)), uses the ITK [40] and MPI [41] libraries, and is fully implemented in Python.

The knowledge on the scattering pattern of X-rays is harnessed to reduce computational complexity by optimising the number of simulated photons per projection and the number of projections themselves. Previous research by Colijn et al. [42] offered foundational insights into accelerating simulations by exploiting the spatial smoothness of scatter signals. However, self-absorption of scattered radiation by the object potentially leads to higher scatter frequencies for complex object shapes. Building upon this foundation, the simulation software is utilised for determining how many photons will give a reliable measure of scattered radiation, to identify the minimal number of photons needed to simulate each projection. This is done by monitoring the power of the spatial scatter signal (see Fig. 3) for the first projection, for increasing number of simulated photons. As the photon count at each pixel increases along with the signal-to-noise ratio of the scatter signal, the bandwidth Ω_m of the scatter signal (representing the highest frequency encompassing 95% of the total power within $[0, \Omega_m]$) gradually converges to a stable value (as determined experimentally in Section 4.1). The number of photons determined in this way was used for all subsequent projections. As a consistent part of the scatter signal is contained in Ω_m, the rest of the spectrum can be cleaned from the MC noise with a low-pass Butterworth filter, known for its maximally flat response in the passband Ω_m. By utilising the filter as a zero-phase filter, the filter order is chosen as the lowest order necessary to achieve a maximum power suppression of 0.025 dB in the Ω_m-band, along with a minimum −30 dB power suppression of frequencies beyond the stopband Ω_s, which is 10% higher than Ω_m. These numeric values that select the filter order were found to be sufficient for the denoising task.

By exploiting the temporal smoothness of the scattered radiation on the detector pixels (i.e., smoothness between subsequent projections, see Fig. 3), the computational burden of simulating the entire X-ray projection stack is reduced to the simulation of just a few projections. These few scatter estimates, through Fourier interpolation, provide the X-ray scatter estimates corresponding to all other projections. This is

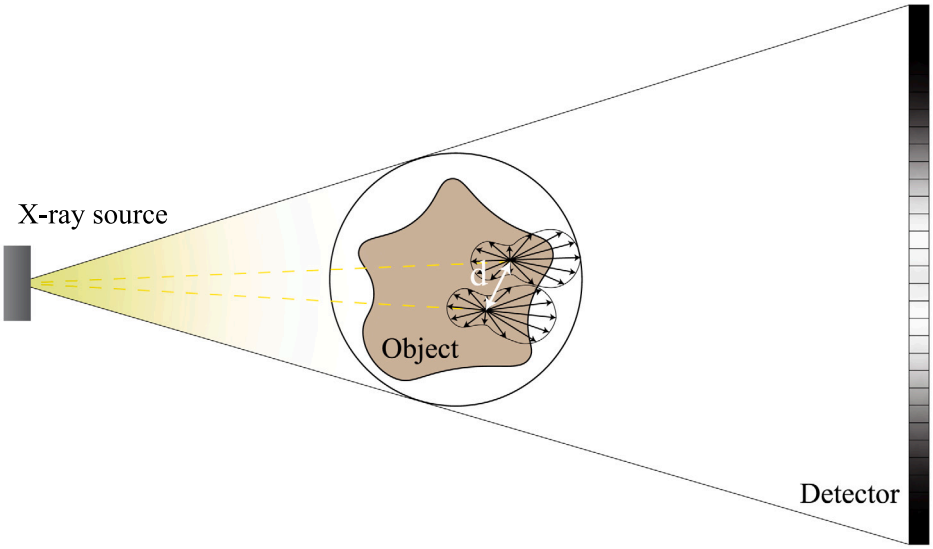

Fig. 4. The X-ray scatter footprint of a minuscule region of the scanned object exhibits low spatial frequencies in conventional X-CT acquisition setups. This makes two scattering regions indiscernible if they are close enough, despite the linear absorption associated with these regions being resolved by the tomographic reconstruction.

a substantial difference from previous works [23,25,43], where scatter estimates were computed using linear interpolation, and the selection of key projections was done manually. In principle, nearby scattering regions of the scanned object at a distance d may not be clearly discernible from their scatter footprint (Fig. 4). Consequently, during an X-CT reconstruction that ignores the scattered radiation in the forward model (e.g. FDK, SART, SIRT), the scatter-affected projections drive the reconstructed volume to be explanatory of the (mainly low) spatial frequencies of the scatter signal, as well as the scatter signal variation among projections. By sub-sampling these projections, the variation of the scatter signal among these projections can be constrained to have the same impact on the reconstruction as for the spatial scatter signal. In case of circular cone-beam computed tomography (CBCT), the constraint is imposed through known relations [44], based on the data completeness theorem for the central cross-section [45], which establish a connection between spatial sampling and angular sampling for reconstructing a given object. Let $g(x, y) \in \mathbb{R}$ indicate the linear attenuation of said object, contained in a circle of radius r, such that $g(x, y) = 0; \forall (x, y), \in \mathbb{R}^2, |\sqrt{x^2 + y^2} \geq r$. Assuming that the spectral band of g can be reasonably Ω_g-limited (as is commonly done for X-CT reconstructions [44,46]), it follows that a condition on the minimal number of samplings along each view is necessary to recover the Ω_g-limited g [44]:

$$\Delta y \leq \frac{\pi}{\Omega_g} \quad . \tag{3}$$

Here, Δy represents the scaled spacing between pixels on the flat detector, measured relative to the object centre ($\Delta y = \Delta s \cdot \frac{R}{D}$, where R is the source-to-object distance and D the source-to-detector distance), where Δs denotes the spacing between pixels. Moreover, to ensure that g can be fully recovered, the angular spacing $\Delta\beta$ among views of the circular trajectory must also satisfy the inequality [44]:

$$\Delta\beta \leq \frac{\pi}{r\Omega_g}\left(\frac{R+r}{R}\right)\left(1-\frac{r^2}{R^2}\right) \quad . \tag{4}$$

Given that the spatial bandwidth Ω_m of the scattered radiation is already established, the object bandwidth Ω_g that described the spatial scatter is linearly determined and consequently constrains the angular sampling, as indicated by (4). Finally, after determining the subset of X-ray projections to simulate using this angular sampling, resampling in Fourier space provides the missing estimates for scatter.

Variance reduction techniques in MC simulations of X-ray photons are known to improve the efficiency of the simulations. These methods strategically allocate computational resources to areas where interactions are most important, reducing statistical noise. As these techniques may introduce a bias in scatter estimates, which is adversary to the scope of the study, they are not used here.

3.3. X-ray scatter compensation

After obtaining the estimate of scattered radiation, the next step is to compensate for the scatter in the projections. It is important to note that the measured and simulated projections depend on the number of photons physically generated and simulated, respectively. Additionally, the presence of dark currents affecting the measured projections must be properly handled during X-ray scatter compensation — a factor that was overlooked in previous studies [22–25]. To address these factors, the following corrections are applied.

First, we correct the projections $\boldsymbol{P}$ using the white-field $\boldsymbol{W}$ and dark-field $\boldsymbol{D}$ images to account for gain and dark currents. This results in $\boldsymbol{P}_{corr} = (\boldsymbol{P} - \boldsymbol{D})/(\boldsymbol{W} - \boldsymbol{D})$. Similarly, we apply the same correction to the simulated projections, which do not have dark currents, leading to $\hat{\boldsymbol{P}}_{corr} = \hat{\boldsymbol{P}}/\hat{\boldsymbol{W}}$ and $\hat{\boldsymbol{S}}_{corr} = \hat{\boldsymbol{S}}/\hat{\boldsymbol{W}}$. In the absence of scatter, the dynamic range of $\boldsymbol{P}_{corr}$ and $\hat{\boldsymbol{P}}_{corr}$ would be within to the interval [0, 1]. However, the presence of scattered radiation causes some pixel values to exceed 1. Since a portion of the absolute value of $\boldsymbol{P}_{corr}$ and $\hat{\boldsymbol{P}}_{corr}$ is attributed to scattered radiation, this scattered radiation is compensated in the measured projections with $\boldsymbol{P}_{sc} = \boldsymbol{P}_{corr} - \hat{\boldsymbol{S}}_{corr}$. Finally, the dynamic range of the measured projections can be restored by reversing the white/dark-field correction using $\boldsymbol{P} = \boldsymbol{P}_{sc}(\boldsymbol{W} - \boldsymbol{D}) + \boldsymbol{D}$ and are ready for reconstruction.

4. Experiments

The three experiments presented in this section are conducted sequentially, with the information gathered from experiments in Sections 4.1 and 4.2 serving as a foundation for the last one (Section 4.3). After determining the optimal number of photons required for a reliable estimation and establishing the bandwidth of the X-ray scattering signal to downsize the simulation task (Section 4.1), the next step involves multi-mesh registration and adaptation based on a minimal set of X-ray projections (dataset 10P), as detailed in Section 4.2. This step enables the subsequent simulation and compensation of X-ray scattering from the scanned X-ray projections 4.3.

4.1. Spatial frequencies of X-ray scatter on the detector

In this experiment, the scattered radiation of the scanned sample is measured through simulations that were run with different number of photons (10^9, 10^{10}, …, 10^{13}), with the information provided in Sections 2 and 3.2. The aim of the experiment is two-fold: to find the number of photons to be used for a reliable estimation of the X-ray scattered radiation for the X-ray scan, and to find the bandwidth of the X-ray scattered signal. The latter is used to determine the angular downsampling of the X-ray scatter simulations. The analysis is conducted in the frequency domain, where we define the bandwidth Ω_m of the X-ray scattered radiation as the band in which 95% of the power is contained.

4.2. Multi-object pose and shape estimation

In this experiment, the aim is to infer the pose of the objects (the gear and its supporting elements) from the scanned X-ray projections and to adapt any surface mesh to the corresponding object, to compensate for deformation arising from a non-ideal 3D printing process. The operation is conducted in two subsequent phases. First, the pose of the object is estimated through minimisation of the linear programming problem (1) while the poly-chromatic behaviour of the source and detector are continuously estimated jointly with the object pose. Then, while the spectral behaviour and the pose remain fixed, the linear programming problem described with (2) is optimised by adjusting the vertices' positions in order to account for the objects' deformations. The optimisation of both the linear programming problems is performed with the lowest number of projections (dataset 10P).

4.3. X-ray scatter compensation

In this experiment, the surface meshes of all the components of the X-ray scene, along with their chemical composition information, are used for the compensation of the X-ray scattered radiation. The full compensation procedure is described in Section 3.3. This process was systematically applied to all datasets, and the outcomes were analysed according to the inspection scenario — whether it is projection-based inspection, X-CT inspection using discrete reconstruction, or conventional X-CT inspection. Projection-based inspection, suitable for rapid assessments where tomographic information is unnecessary, relies on the sparse set of projections from the 10P dataset. In contrast, X-CT inspection with discrete reconstruction offers enhanced analysis and tomographic visualisation of internal features and defects compared to projection-based methods, leveraging the denser 100 equiangularly sampled projections of the 100P dataset. Conventional X-CT inspection, providing the highest level of tomographic detail and resolution for precise reconstruction, is employed when thorough examination and accurate measurement are imperative, despite the increased computational and time demands. This method utilises the extensive data from the 3000P dataset. Specifically, for projection-based and conventional X-CT inspection inspections, the results are supplemented with an assessment of residual errors using the mesh-projector (cfr. Section 4.2). In each case, the obtained results were benchmarked against the performance of a recent flavour of scatter kernel superposition method [10] for scatter compensation.

5. Results and discussions

5.1. Spatial frequencies of X-ray scatter on the detector

Fig. 5 shows the results of simulation runs with increasing number of photons, and all replicating the same geometrical setup of a scanned X-ray projection. More in-depth insights can be obtained from Fig. 6, which shows the power spectrum of the detector readout. As expected, the white noise related to the MC-statistics diminishes its power by 10 dB for every order of magnitude of the number of simulated photons. As a consequence, the 95% of the power of the detected signal falls between a smaller bandwidth, as the number of photons increase, which is in accordance with the literature affirming that scattered radiation is mostly composed of low-frequencies. The 95% power bandwidth is reported in Table 1 and shows that after a certain number of simulated photons (10^{11}), the bandwidth of the signal does not vary anymore. This is the lowest number of photons that is simulated during the simulation of each projection during the scatter compensation phase. The related bandwidth has been used to set up the low-pass filter, which led to Fig. 7(a). For this bandwidth, the number of projections to be simulated during the scatter compensation phase, as selected according to Eq. (4), is 30, which resulted in almost 11 h of computation time with 2048 cores (AMD Epyc 7452).

5.2. Multi-object pose and shape estimation

The optimisation of the linear programming problem (1) refined the initial pose of the objects within the scanned scene, which is noticeable in Fig. 8 from residual images (i.e. difference between simulated projections and scanned projections) and measures of the Root Mean Squared residuals (RMSres). Starting from the initial object pose configuration that resulted in high projection errors (Fig. 8(a)), the optimisation led to improved spatial positioning of the objects (Fig. 8(b)), highlighting a significant reduction in projection-wise error. However, some regions in the post-registration image still exhibit high errors, which can be attributed to actual 3D printing deformations.

By optimising the linear programming problem (2), the surface meshes of the CAD model were adjusted to match the true shape of the 3D printed objects (Fig. 8(c)). A visual representation of this deformation is provided in Fig. 9, where the displacement of each vertex is measured as Euclidean distance, influencing the heatmap colour representation in the figure.

The execution times for the registration and shape adaptation procedures proved to be robust even as the number of vertices in the scanned object increased (Table 2). These timings are inherently influenced by the forward and backward passes of the mesh projector, which have been extensively analysed in previous work [27]. The accuracy and reliability of pose estimation, using varying numbers of projections, have been thoroughly investigated and documented in a recent publication [47]. To further explore shape estimation accuracy, an additional analysis was conducted using the 100P dataset. The results of this analysis are available in the supplementary files and show deviations of the order of 10 µm.

5.3. X-ray scatter compensation

In Fig. 10, an analysis of the scatter compensation for the projection from the dataset 10P in projection space is presented. Despite the visual similarity between the chosen projection and its scatter-compensated versions, certain details are more apparent in the residual images. These images depict the absolute residual between the dark/white-field corrected X-ray projections and the poly-chromatic projections of the meshes.

Examining the images in Fig. 10, the central part of the residual image for a measured projection (Fig. 10(b)) reveals a whitish halo. This halo is less pronounced in the scatter-compensated projection using the Scatter-Kernel Superposition (SKS) method [10], as noticeable in Fig. 10(d), and almost imperceptible in the scatter-compensated projections using PACS (Fig. 10(f)). Additionally, all residual images (Fig. 10(b), 10(d) and 10(f)) display the general shape of the scanned sample, resulting from minor inaccuracies in mesh estimation. Furthermore, two macroscopic defects can be observed. Close-ups and line profiles of these macroscopic defects, provided in Fig. 11, indicate that the scatter-affected projection has a non-zero value even outside the defective zone. These values arise from the mismatch between the

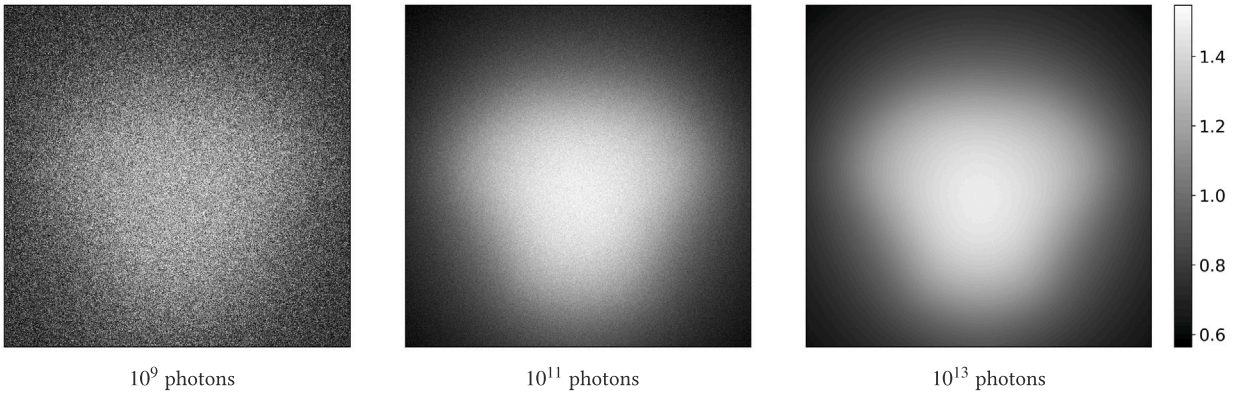

Fig. 5. Rayleigh and Compton scatter for different numbers of simulated photons, divided by the average value.

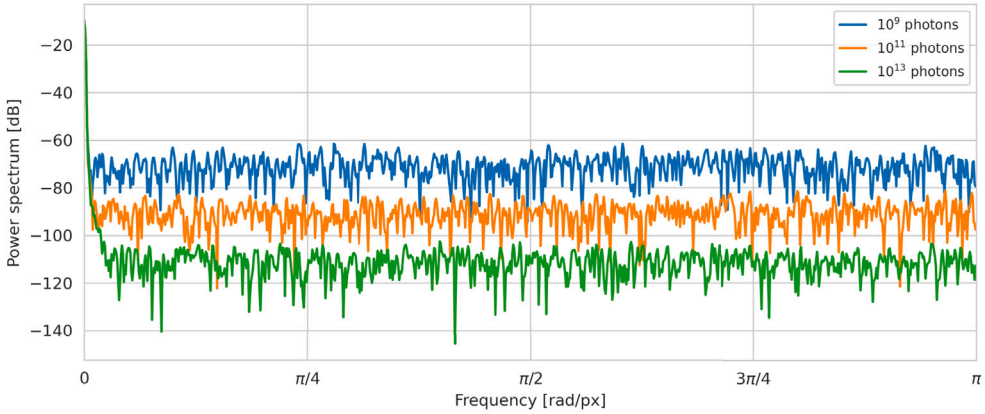

Fig. 6. One-sided power spectrum, extracted from the vertical distribution of frequencies of the 2-D Fourier space, for the scattered radiation shown in Fig. 5. The white-noise, related to the MC-statistics, lowers its power with higher number of photons, while the low-frequency scatter components become noticeable.

Table 1
The 2D bandwidth of the scattered radiation, which contains 95% of the total power, is reported here for different numbers of simulated photons.

	10^9 photons	10^{10} photons	10^{11} photons	10^{12} photons	10^{13} photons
Ω_m [rad/px]	3.138	9.942e−03	6.628e−03	6.628e−03	6.628e−03

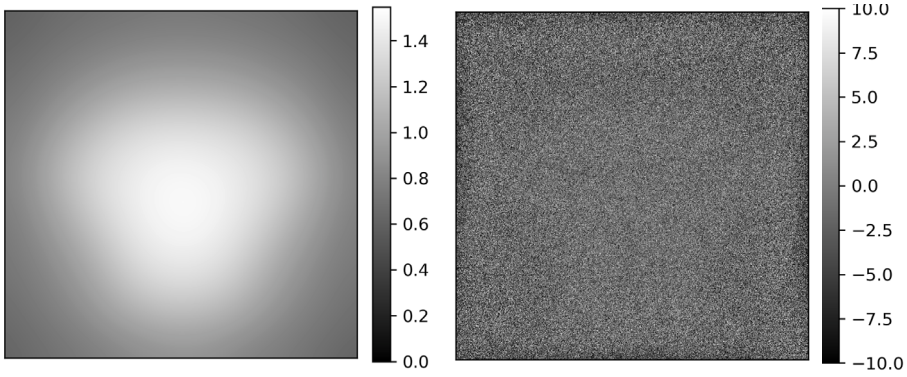

(a) Filtered image (10^{11} photons) (b) Percent-wise relative error

Fig. 7. (a) The X-ray projection after application of the Butterworth filter, using 10^{11} photons, and (b) the relative difference between the filter and related unfiltered image, showing that only the MC-white noise has been removed by the filter.

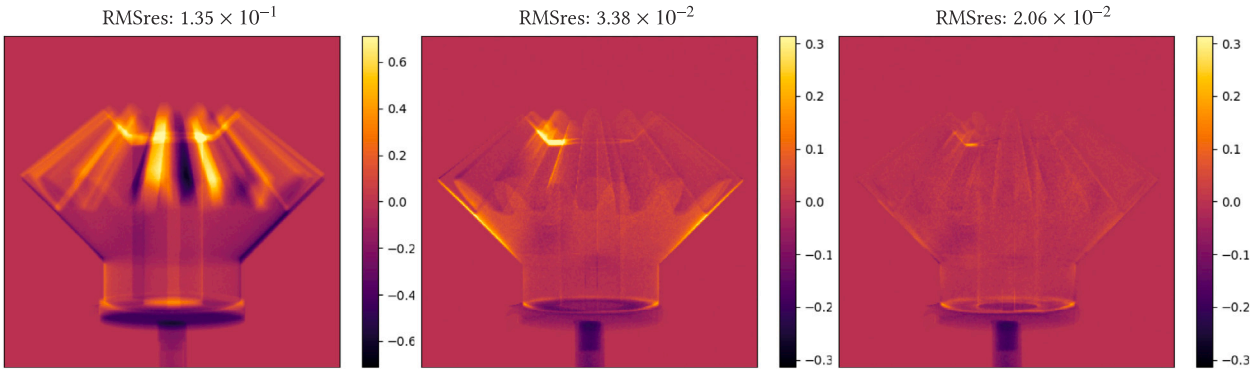

(a) Before registration (b) After registration (c) After mesh adaption

Fig. 8. Residual images of the bevel gear and its supporting elements for three different instants of the multi-mesh registration/adaption procedure. The figure shows how an initial pose guess of the various elements can be adapted to the actual scan, while accounting for deformations, in an automatic way.

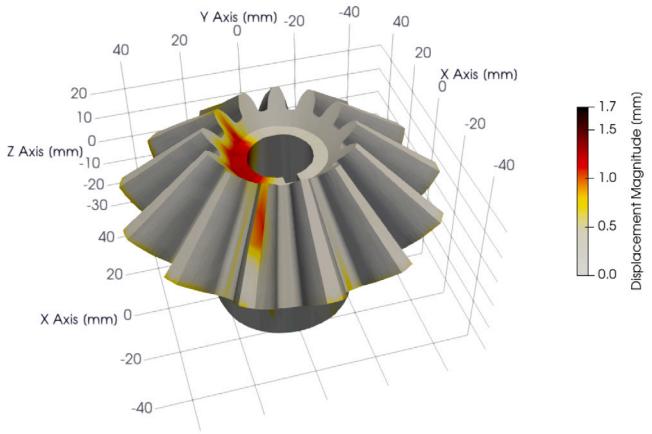

Fig. 9. The difference between the surface mesh of the CAD model to the actual object is considered to arise from a faulty 3D printing process, for which a heatmap of the Euclidean displacement of surface mesh vertices provides a clearer visualisation of the deformed shape, compared to the projection-wise representation of Figs. 8(b) and 8(c).

Table 2
Execution times for the registration and shape adaption by varying the number of mesh vertices of the main scanned object.

# vertices	6 875	13 807	55 696	223 353
Registration time [s]	214.63	198.83	199.56	199.99
Shape estimation time [s]	168.64	155.68	157.12	163.66

actual object surface and its surface mesh. To quantitatively evaluate the performance of the scatter compensation methods of the results shown in Figs. 10 and 11, the RMSres is computed along with its standard deviation and it is reported in Table 3. This evaluation, encompassing all projections in dataset 10P, highlights that PACS yields the least amount of residuals than the SKS method.

With the dataset 100P, a discrete X-CT reconstruction is performed with a voxel-size of 100 µm. Employing this technique enables the creation of a (voxel-wise) multi-label volume, offering a three-dimensional discrete representation, as depicted in Fig. 12. The application of this technique highlights macroscopic defects more distinctly, as observed in the images in Fig. 13(b), 13(f) and 13(h). Furthermore, it allows for the detection of pores within the X-CT. However, in practice, the presence of imaging noise and scattered radiation may lead to the identification of spurious pixels unrelated to real pores.

In Fig. 13, the 3D rendering visually displays the distribution of spurious pores in the reconstructed volume. Notably, scatter-compensated projections result in a reduced occurrence of these defects. The number of detected pores and their similarity to the voxel-wise manually-labelled ground truth of pores are quantified and presented in Table 4. The similarity is measured using the Dice-Sørensen coefficient, a statistical tool used to gauge the spatial overlap between two segmentation masks. Specifically, it assesses the agreement between the detected defects and the ground truth, thereby providing a quantitative measure of the segmentation accuracy. This analysis demonstrates that scatter compensation significantly enhances the fidelity of pore representation, with PACS outperforming SKS in terms of the Dice-Sørensen coefficient. The reason for higher concentration of detected pores in the top part of the gear is related to X-ray scattering artefacts, and it is explained by using the dataset 3000P, where more information can be extracted from X-ray projections.

Utilising the complete set of projections (dataset 3000P) allows for regular X-CT reconstruction, ensuring faithful results. As for the previous case, the voxel-size is 100 µm. In Fig. 14, a cross-section analysis of the poly-BB reconstruction is presented in a region previously identified as challenging for poly-DART. The line plot in the figure illustrates that the standard deviation and average gray values of poly-BB are smaller for scatter-compensated images, providing an explanation for the spurious pores detected with the 100P dataset. These values, evaluated across the volumetric gear region, are detailed in Table 5. A consequence of the higher signal-to-noise (SNR) value is that the contrast of pores is enhanced. This is evaluated across all pores and reported in Table 6, through their contrast-to-noise (CNR) ratio, which confirmed the expectations.

Examining the residual values (Fig. 15) offers a deeper insight into the results observed in Figs. 13 and 14. The presence of spurious pores (Fig. 13) and the additional noise and non-constant trend of line profiles (Fig. 14), unexpected for a homogeneous material, is attributed to X-ray scattering artefacts. These artefacts gradually diminish with the application of scatter-compensation techniques. The evaluation of average absolute residuals, confirming the visual findings, is reported in Table 7.

6. Conclusions

A new approach (PACS) was proposed to accurately compensate for X-ray scatter in projection images. This method involves registering and adapting CAD models of AM objects, followed by a Monte Carlo simulation of X-ray scatter in the projections, and then compensating for it in the actual radiographs. Results demonstrated that accurate registration of CAD models is possible using only few projections, rendering simulation-based X-ray scatter compensation approaches a viable option in scenarios where few projections are available or desirable. The adaptability of such approach addresses common constraints

Table 3
Measure of the mean squared residual throughout all projections of dataset 10P. The residual is interpreted as the difference between the projections and the simulated poly-chromatic projections.

	Unprocessed	SKS	PACS
RMSres	$(3.778 \pm 0.046) \times 10^{-2}$	$(2.094 \pm 0.046) \times 10^{-2}$	$\mathbf{(1.539 \pm 0.044) \times 10^{-2}}$

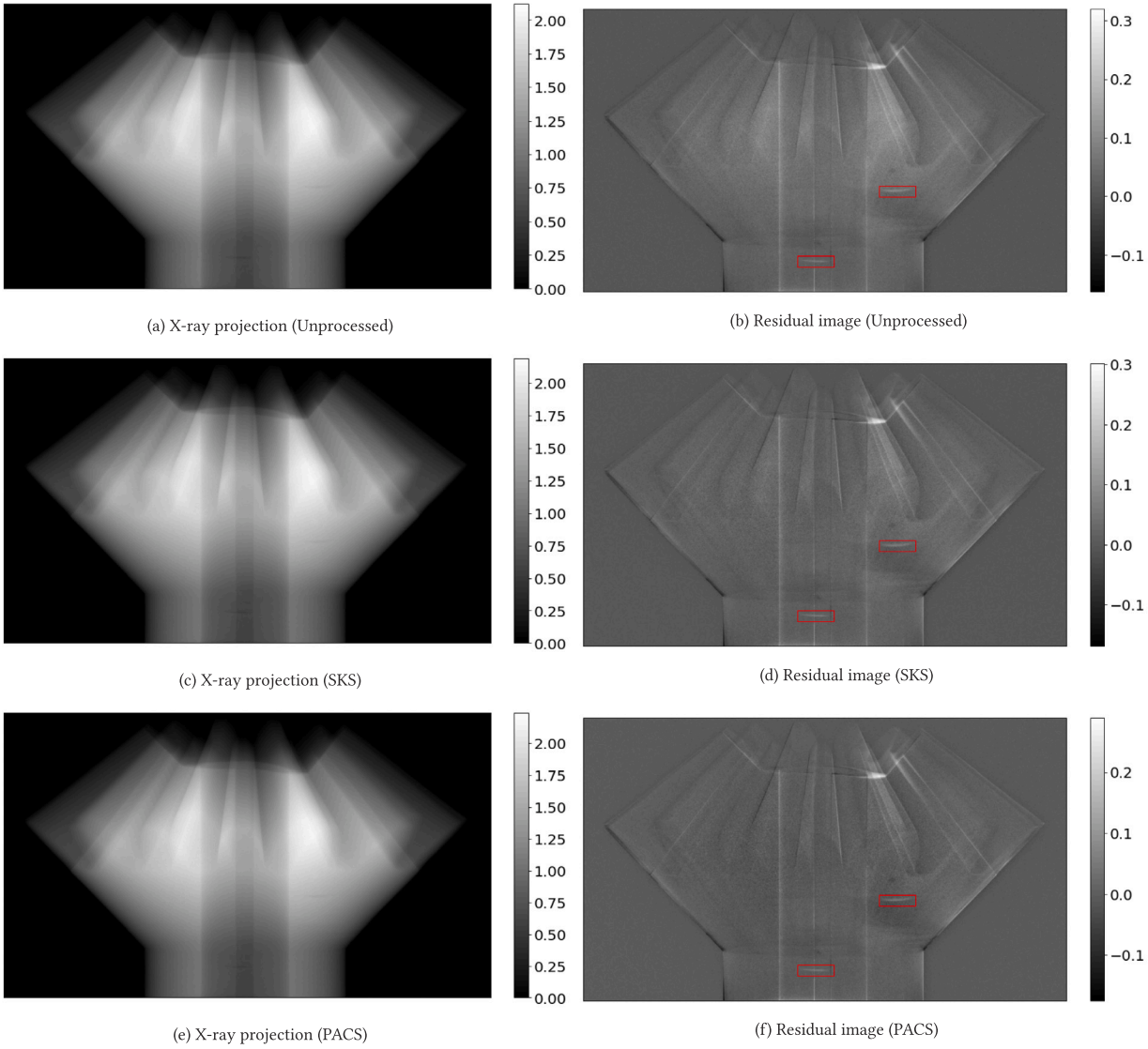

(a) X-ray projection (Unprocessed)

(b) Residual image (Unprocessed)

(c) X-ray projection (SKS)

(d) Residual image (SKS)

(e) X-ray projection (PACS)

(f) Residual image (PACS)

Fig. 10. X-ray projections are presented on the left for three cases: (a) without scatter correction, (c) with scatter correction using SKS, and (e) with scatter correction using PACS. Accompanying these, the residual images are depicted as (b) uncorrected, (d) corrected with SKS, and (f) corrected with PACS. Two red boxes highlight macroscopic defects for a detailed analysis in Fig. 11.

Table 4
Measure of the number of detected pores through the poly-DART reconstruction of the few projections of dataset 100P. The similarity of the detected pores with those of the ground truth is measured with the Sørensen–Dice score.

	Unprocessed	SKS	PACS
# of pore-voxels	1816	1001	368
Sørensen–Dice coefficient	0.061	0.069	**0.074**

encountered in industrial scanning setups, including throughput, cost, and spatial limitations. Replacing the CAD model with another object before scanning, in response to changing industrial needs, incurs no additional overhead compared to alternative methods. Furthermore, this method, inherently coupled with a mesh projector, allows for the analysis of residual differences between real and simulated projections. This feature facilitates the identification of deformities or defects within the scanned object.

Multiple experiments consistently demonstrate superior accuracy in X-ray scattering artefact reduction of PACS compared to one of the latest SKS scatter compensation methods. The absence of training procedures and the ability to easily adapt to any scanned object make PACS the method of choice for scans in the context of AM. As PACS relies on Monte Carlo simulations for X-ray scatter compensation, strategies to reduce the computational load were investigated. However, employing GATE as a simulation backend remains computationally intensive,

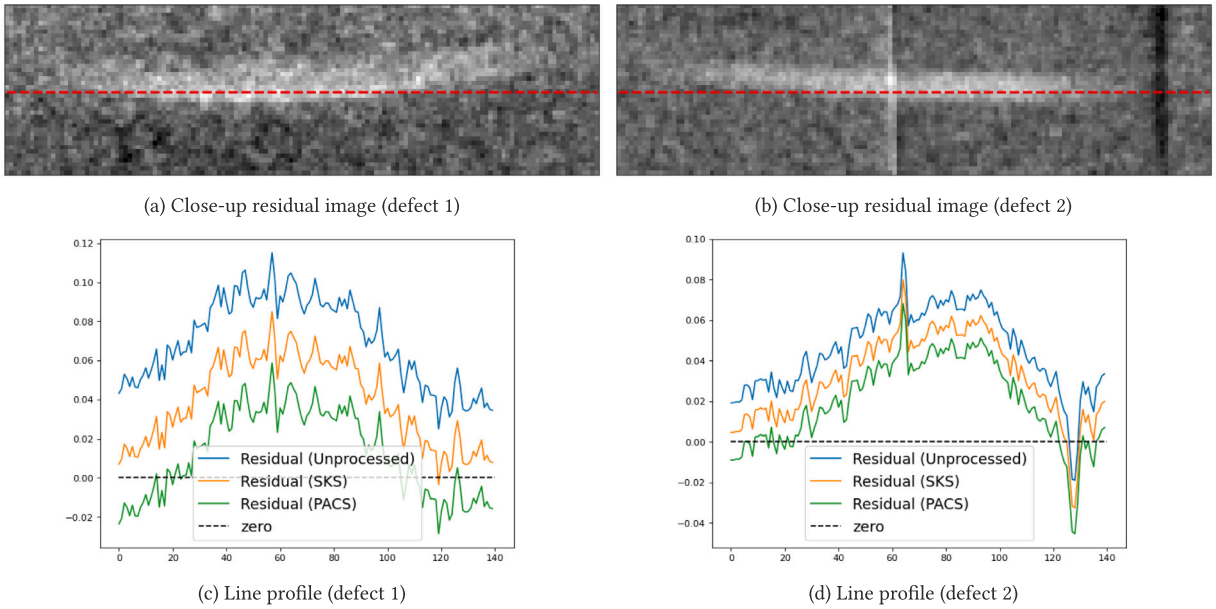

(a) Close-up residual image (defect 1)

(b) Close-up residual image (defect 2)

(c) Line profile (defect 1)

(d) Line profile (defect 2)

Fig. 11. Close-ups of two defects highlighted in the residual images of Fig. 10. Line profiles through these close-ups reveal the varying behaviour of residual gray values across the defects, where it is desirable that high values are associated with the defective area, while zero values are associated with the absence of defects.

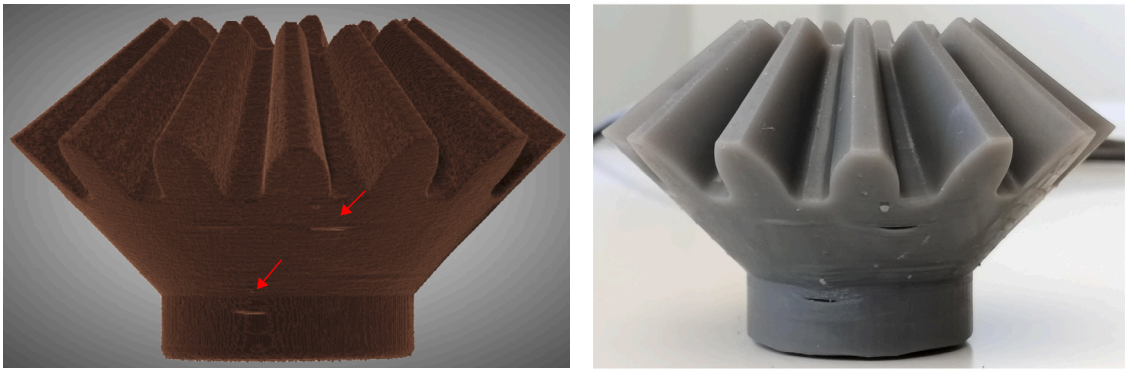

(a) Poly-DART reconstruction

(b) Two macroscopic 3D printing defects

Fig. 12. From the limited data in the 100P dataset, the binary poly-DART reconstruction (a) of the bevel gear holds meaningful information, as for the 3D printing defects (b).

Table 5
Measure of the average gray value level and SNR throughout the bevel-gear region of the poly-BB reconstruction of dataset 3000P, for unprocessed X-ray projections, SKS scatter-compensated projections and the scatter-compensated projections with PACS.

	Unprocessed	SKS	PACS
Gray value	$(2.654 \pm 0.001) \times 10^{-2}$	$(2.719 \pm 0.001) \times 10^{-2}$	$(2.768 \pm 0.001) \times 10^{-2}$
SNR	87.2	92.6	**96.9**

Table 6
Measure of the average CNR of pores in the poly-BB reconstructions of the uncorrected, SKS scatter-compensated and scatter-compensated projections with PACS, for the dataset 3000P.

	Unprocessed	SKS	PACS
Average CNR	4.23 ± 0.37	4.45 ± 0.40	**4.70 ± 0.40**

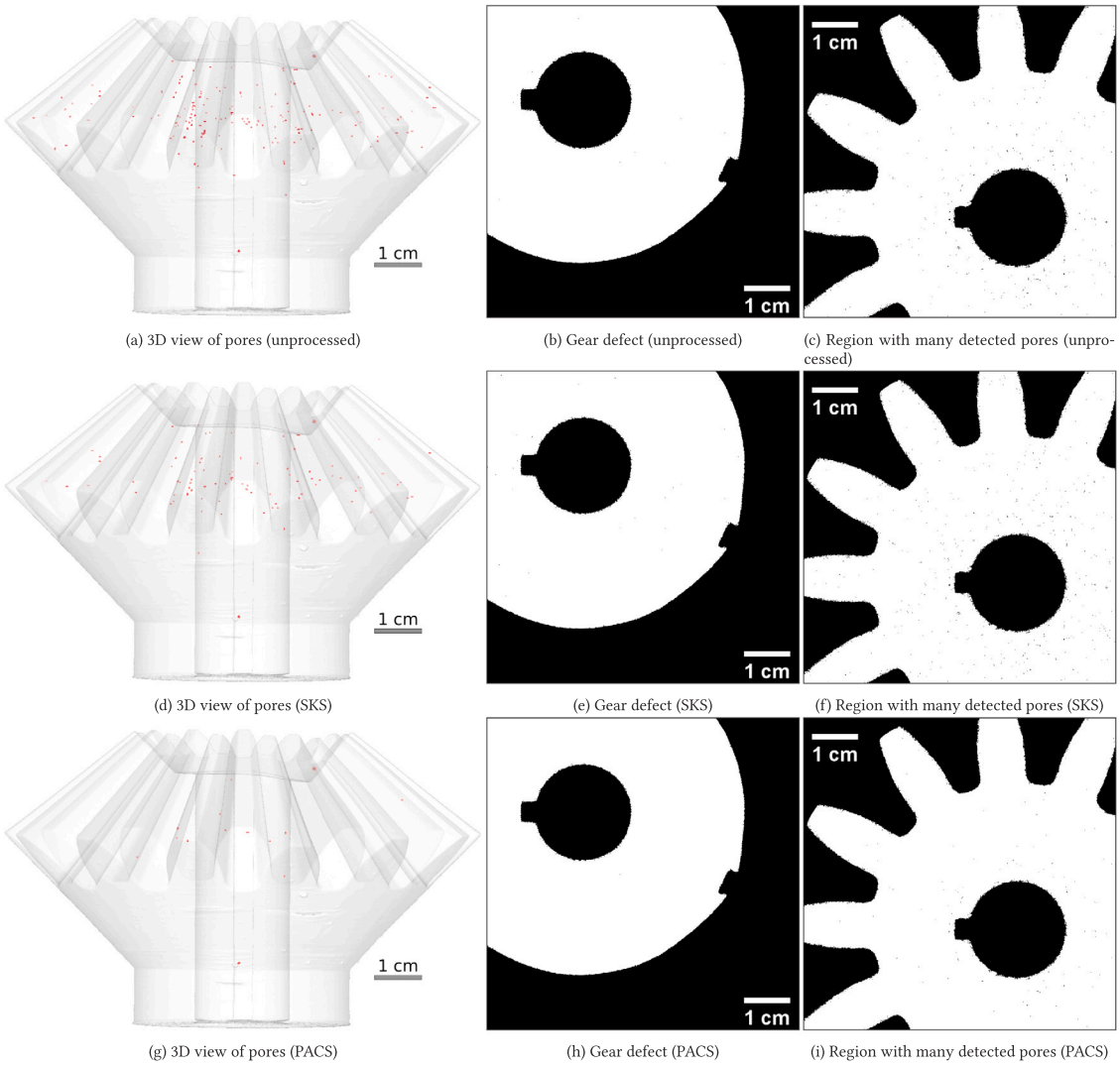

(a) 3D view of pores (unprocessed) (b) Gear defect (unprocessed) (c) Region with many detected pores (unprocessed)

(d) 3D view of pores (SKS) (e) Gear defect (SKS) (f) Region with many detected pores (SKS)

(g) 3D view of pores (PACS) (h) Gear defect (PACS) (i) Region with many detected pores (PACS)

Fig. 13. Comparison of Poly-DART reconstructions: unprocessed X-ray projections (a–c), scatter-compensated with SKS (d–f), and scatter-compensated projections with PACS (g–i). The 3D visualisation (a,d,g) highlights all detected pores within the Poly-DART reconstruction, with a visibly higher number in the top part of the bevel gear. The images (b,e,h) show a cross-section with the correct reconstruction of a defective area, while the (c,f,i) images focus on the variable number of pores detected by each Poly-DART reconstruction. The correlation of the detected pores with the ground truth is shown in Table 4.

Table 7
Measure of the root mean squared residual throughout the dataset 3000P. The residual is interpreted as the difference between the poly-BB reconstruction and the simulated poly-BB reconstruction in the space occupied by the gear.

	Unprocessed	SKS	PACS
RMSres	$(3.146 \pm 0.034) \times 10^{-3}$	$(2.909 \pm 0.035) \times 10^{-3}$	$\mathbf{(2.819 \pm 0.035) \times 10^{-3}}$

which can be further reduced using modern GPU solutions specialised in X-ray scatter simulations, as presented in recent works [23].

A noteworthy future prospect arising from this work is the development of an X-ray scatter estimation pipeline that would rely solely on the mesh projector. Coupling the mesh projector with an analytical description of the 1st order scatter [48], evaluated across the entire surface mesh, is expected to yield significant improvements in speed. This is particularly true in cases where the inspected object is small, or the detector is positioned sufficiently far from the X-ray source.

CRediT authorship contribution statement

Domenico Iuso: Writing – original draft, Software, Conceptualization. **Pavel Paramonov:** Writing – review & editing, Software. **Jan De Beenhouwer:** Writing – review & editing, Supervision. **Jan Sijbers:** Writing – review & editing, Supervision.

Declaration of competing interest

The authors declare that they have no known competing financial interests or personal relationships that could have appeared to influence the work reported in this paper.

Acknowledgments

We gratefully acknowledge Joaquim Sanctorum for his assistance in performing the CT scan for this study. This study is financially supported by the VLAIO/imec-ICON project Multiplicity (HBC.2022.0094), the Research Foundation - Flanders (FWO, SBO project S007219N) and it has partially utilised resources from VSC (Flemish Supercomputer Center), funded by the FWO and the Flemish Government.

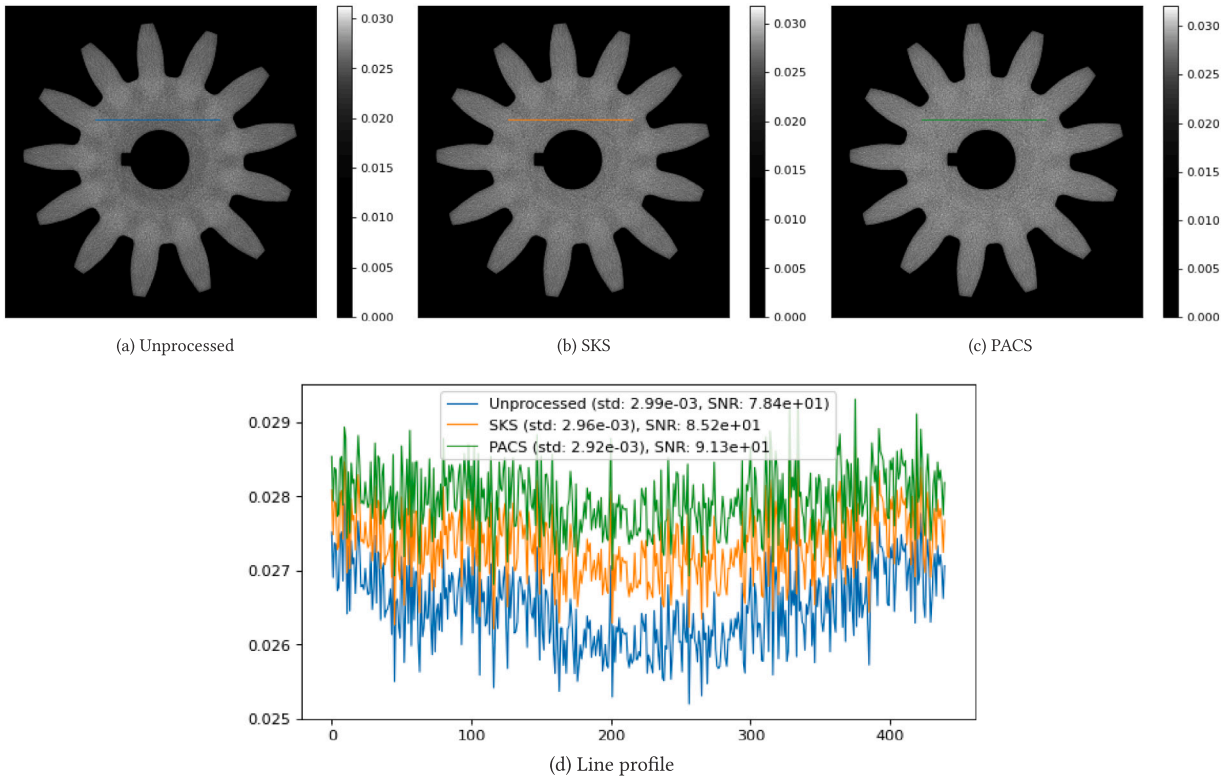

(a) Unprocessed (b) SKS (c) PACS

(d) Line profile

Fig. 14. A cross-section of the poly-BB reconstruction of (a) unprocessed X-ray projections, (b) SKS scatter-compensated projections and (c) the scatter-compensated projections with PACS of the complete 3000P dataset.

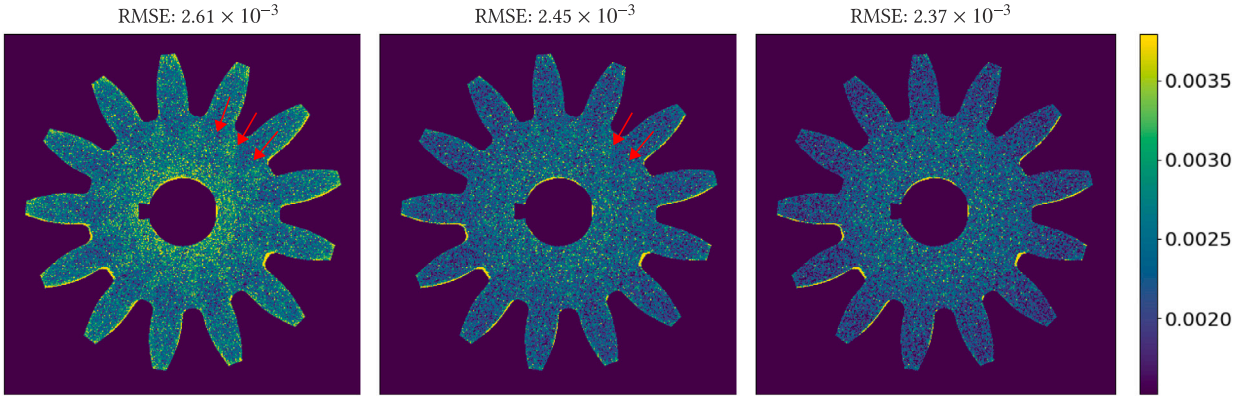

(a) Unprocessed (b) SKS (c) PACS

Fig. 15. Cross-sections of residual poly-BB reconstructions from the complete 3000P dataset: (a) unprocessed X-ray projections, (b) SKS scatter-compensated projections, and (c) scatter-compensated projections with PACS. Red arrows indicate areas with noticeable artificial trends in the residuals. The Root Mean Squared Error (RMSE) for each image is shown at the top of the corresponding figure.

Appendix A. Theoretical white-field image for flat detectors

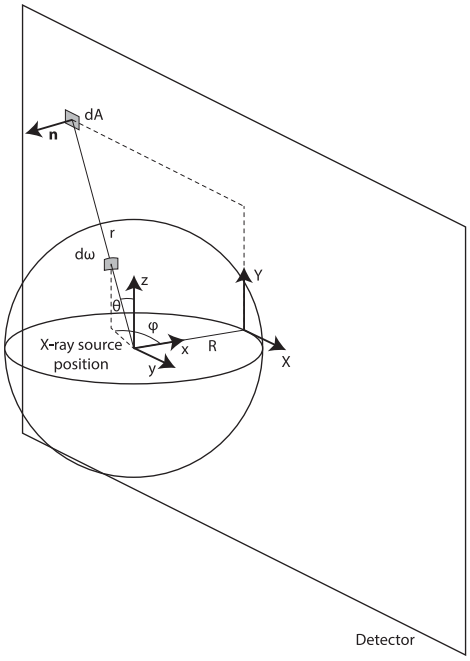

This section provides a practical approximation for the amount of radiation crossing a detector pixel in the case of isotropic X-ray emission.

Assuming isotropic X-ray emission with total emission denoted as J^*, the emission per steradian is a constant referred to as $J = J^*/4\pi$. The radiation crossing a detector pixel p is given by the integration of the emission J over the solid angle $d\omega$ related to the detector pixel area A_p:

$$I_p = \int_{A_p} J\, d\omega \quad , \tag{A.1}$$

where I_p represents the radiation crossing p. The infinitesimal $d\omega$ is linked to the infinitesimal area da through $d\omega = \boldsymbol{n} \cdot \hat{\boldsymbol{v}}\, da/r^2$, with $\boldsymbol{n}$ being the detector pixel normal and $\hat{\boldsymbol{r}}$ the versor of the line r connecting the detector pixel center and the X-ray source position. As the versor $\hat{\boldsymbol{r}} = (x, y, z)$ has components

$$\begin{cases} x = \sin\theta\cos\phi \\ y = \sin\theta\sin\phi \\ z = \cos\theta \end{cases} \quad , \tag{A.2}$$

then it is possible to rewrite Eq. (A.1) as

$$I_p = J \int_{A_p} \frac{\boldsymbol{n}\cdot\hat{\boldsymbol{v}}}{r^2} da = J \int_{A_p} \frac{\sin\theta\cos\phi}{r^2} da\,, \tag{A.3}$$

and, expressing it in terms of the position of the detector pixel center $P(X_p, Y_p)$, it becomes

$$I_p = J \int_{A_p} \frac{R\, da}{(R^2 + X_p^2 + Y_p^2)^{\frac{3}{2}}} \quad . \tag{A.4}$$

Under the assumption that the detector distance R from the source is much greater than X_p and Y_p and of the pixel area A, then the denominator is nearly constant throughout the integration on the pixel area and it can be brought outside the integration. This allows us to conveniently approximate Eq. (A.4) with

$$I_p \approx \frac{J\, A\, R}{(R^2 + X_p^2 + Y_p^2)^{\frac{3}{2}}} \quad . \tag{A.5}$$

Appendix B. Supplementary data

Supplementary material related to this article can be found online at https://doi.org/10.1016/j.precisioneng.2024.08.006.

References

[1] Nielsen M-A, Gloy JF, Lott D, Sun T, Müller M, Staron P. Automatic melt pool recognition in X-ray radiography images from laser-molten Al alloy. J Mater Res Technol 2022;21:3502–13.

[2] Du Plessis A, Yadroitsev I, Yadroitsava I, Le Roux S. X-ray microcomputed tomography in additive manufacturing: a review of the current technology and applications. 3D Print Addit Manuf 2018;5(3):227–47.

[3] Sorenson JA, Floch J. Scatter rejection by air gaps: An empirical model. Med Phys 1985;12(3):308–16.

[4] Liu F, Yang Q, Cong W, Wang G. Dynamic bowtie filter for cone-beam/multi-slice CT. PLoS One 2014;9(7):e103054.

[5] Vogtmeier G, Dorscheid R, Engel KJ, Luhta R, Mattson R, Harwood B, et al. Two-dimensional anti-scatter grids for computed tomography detectors. In: Medical imaging 2008: physics of medical imaging, vol. 6913, SPIE; 2008, p. 1659–69.

[6] Schörner K, Goldammer M, Stephan J. Comparison between beam-stop and beam-hole array scatter correction techniques for industrial X-ray cone-beam CT. Nucl Instrum Methods Phys Res B: Beam Interact Mater Atoms 2011;269(3):292–9.

[7] Love L, Kruger R. Scatter estimation for a digital radiographic system using convolution filtering. Med Phys 1987;14(2):178–85.

[8] Star-Lack J, Sun M, Kaestner A, Hassanein R, Virshup G, Berkus T, et al. Efficient scatter correction using asymmetric kernels. In: Medical imaging 2009: physics of medical imaging, vol. 7258, International Society for Optics and Photonics; 2009, p. 72581Z.

[9] Bhatia N, Tisseur D, Létang J. Scattering correction for industrial CBCT using continuously thickness-adapted kernels at MeV energy range. In: The 4th international conference on image formation in X-ray computed tomography. 2016.

[10] Bhatia N, Tisseur D, Valton S, Létang JM. Separable scatter model of the detector and object contributions using continuously thickness-adapted kernels in CBCT. J X-ray Sci Technol 2016;24(5):723–32.

[11] Mason J, Perelli A, Nailon W, Davies M. Quantitative cone-beam CT reconstruction with polyenergetic scatter model fusion. Phys Med Biol 2018;63(22):225001.

[12] Lee H, Lee J. A deep learning-based scatter correction of simulated X-ray images. Electronics 2019;8(9):944.

[13] Griner D, Garrett J, Li Y, Li K, Chen G. Correction for cone beam CT image artifacts via a deep learning method. In: Medical imaging 2020: physics of medical imaging, vol. 11312, International Society for Optics and Photonics; 2020, p. 113124H.

[14] Nomura Y, Xu Q, Shirato H, Shimizu S, Xing L. Projection-domain scatter correction for cone beam computed tomography using a residual convolutional neural network. Med Phys 2019;46(7):3142–55.

[15] van der Heyden B, Uray M, Fonseca G, Huber P, Us D, Messner I, et al. A Monte Carlo based scatter removal method for non-isocentric cone-beam CT acquisitions using a deep convolutional autoencoder. Phys Med Biol 2020;65(14):145002.

[16] Roser P, Birkhold A, Preuhs A, Syben C, Strobel N, Korwarschik M, et al. Deep scatter splines: Learning-based medical X-ray scatter estimation using B-splines. 2020, arXiv preprint arXiv:2005.03470.

[17] Iskender B, Bresler Y. A physics-motivated DNN for X-Ray CT scatter correction. In: 2020 IEEE 17th international symposium on biomedical imaging. IEEE; 2020, p. 609–13.

[18] Yang K, Burkett Jr. G, Boone J. A breast-specific, negligible-dose scatter correction technique for dedicated cone-beam breast CT: A physics-based approach to improve hounsfield unit accuracy. Phys Med Biol 2014;59(21):6487.

[19] Cui H, Xu G, Zhu L. Local-filtration based scatter correction for conebeam CT Using planning CT as a prior. In: 2019 international conference on medical imaging physics and engineering. IEEE; 2019, p. 1–6.

[20] Ingleby H, Lippuner J, Rickey D, Li Y, Elbakri I. Fast analytical scatter estimation using graphics processing units. J X-ray Sci Technol 2015;23(2):119–33.

[21] Wiegert J, Bertram M, Rose G, Aach T. Model based scatter correction for cone-beam computed tomography. In: Medical imaging 2005: physics of medical imaging, vol. 5745, International Society for Optics and Photonics; 2005, p. 271–82.

[22] Shiroma A, Star-Lack J, Holt K, Hu M, Hoelzer S, Yoon S, et al. Scatter correction for industrial Cone-Beam Computed Tomography (CBCT) using 3D VSHARP, a fast GPU-Based linear Boltzmann transport equation solver. In: 9th conference on industrial computed tomography. 2019.

[23] Maslowski A, Wang A, Sun M, Wareing T, Davis I, Star-Lack J. Acuros CTS: A fast, linear Boltzmann transport equation solver for computed tomography scatter–Part I: Core algorithms and validation. Med Phys 2018;45(5):1899–913.

[24] Xu Y, Bai T, Yan H, Ouyang L, Wang J, Pompos A, et al. TH-A-18C-04: Ultrafast cone-beam CT scatter correction with GPU-Based Monte Carlo simulation. Med Phys 2014;41(6Part31):540–1.

[25] Xia X, Hu X, Han Z, Zhang D, Xu Y, Zou J. Scatter correction in cone beam CT for metal additive manufacturing components. Jom 2019;71:1082–7.
[26] Iuso D, Nazemi E, Six N, De Samber B, De Beenhouwer J, Sijbers J. CAD-Based scatter compensation for polychromatic reconstruction of additive manufactured parts. In: 2021 IEEE international conference on image processing. IEEE; 2021, p. 2948–52.
[27] Paramonov P, Francken N, Renders J, Iuso D, Elberfeld T, De Beenhouwer J, et al. CAD-ASTRA: A versatile and efficient mesh projector for X-ray tomography with the ASTRA-toolbox. Opt Express 2024;32(3):3425–39.
[28] Lorensen WE, Cline HE. Marching cubes: A high resolution 3D surface construction algorithm. In: Seminal graphics: pioneering efforts that shaped the field. Association for Computing Machinery; 1998, p. 347–53.
[29] Six N, De Beenhouwer J, Sijbers J. Poly-DART: A discrete algebraic reconstruction technique for polychromatic X-ray CT. Optics Express 2019;27(23):33670–82.
[30] De Samber B, Renders J, Elberfeld T, Maris Y, Sanctorum J, Six N, et al. FleXCT: A flexible X-ray CT scanner with 10 degrees of freedom. Opt Express 2021;29(3):3438–57. http://dx.doi.org/10.1364/OE.409982.
[31] Barzilai J, Borwein JM. Two-point step size gradient methods. IMA J Numer Anal 1988;8(1):141–8.
[32] Palenstijn WJ, Bédorf J, Sijbers J, Batenburg KJ. A distributed ASTRA toolbox. Adv Struct Chem Imag 2016;2(1):19.
[33] Guillemaud R, Tabary J, Hugonnard M, F A, Gliere A. Sindbad: A multi-purpose and scalable X-ray simulation tool for NDE and medical imaging. 2003.
[34] Badal A, Badano A. Accelerating Monte Carlo simulations of photon transport in a voxelized geometry using a massively parallel graphics processing unit. Med Phys 2009;36(11):4878–80.
[35] Sarrut D, Bała M, Bardiès M, Bert J, Chauvin M, Chatzipapas K, et al. Advanced Monte Carlo simulations of emission tomography imaging systems with GATE. Phys Med Biol 2021;66(10):10TR03.
[36] Kawrakow I. Accurate condensed history Monte Carlo simulation of electron transport. I. EGSnrc, the new EGS4 version. Med Phys 2000;27(3):485–98.
[37] Ay MR, Zaidi H. Development and validation of MCNP4C-based Monte Carlo simulator for fan-and cone-beam X-ray CT. Phys Med Biol 2005;50(20):4863.
[38] Elshemey WM, Elsharkawy WB. Monte Carlo simulation of X-ray scattering for quantitative characterization of breast cancer. Phys Med Biol 2009;54(12):3773.
[39] mpiForGate GitHub repository. 2024, https://github.com/mpiForGate/mpiForGate. [retrieved 26 March 2024].
[40] McCormick M, Liu X, Jomier J, Marion C, Ibanez L. ITK: Enabling reproducible research and open science. Front Neuroinform 2014;8:13.
[41] Dalcin L, Fang Y-LL. mpi4py: Status update after 12 years of development. Comput [S]ci [E]ng 2021;23(4):47–54.
[42] Colijn A-P, Beekman FJ. Accelerated simulation of cone beam X-ray scatter projections. IEEE Trans Med Imaging 2004;23(5):584–90.
[43] Bootsma G, Verhaegen F, Jaffray D. Spatial frequency spectrum of the X-ray scatter distribution in CBCT projections. Med Phys 2013;40(11):111901.
[44] Izen SH. Sampling in flat detector fan beam tomography. SIAM J Appl Math 2012;72(1):61–84.
[45] Wu P, Tersol A, Clackdoyle R, Boone JM, Siewerdsen JH. Cone-beam CT sampling incompleteness: Analytical and empirical studies of emerging systems and source–detector orbits. J Med Imaging 2023;10(3):033503.
[46] Zhao S-R, Jiang D, Yang K, Yang K. Generalized fourier slice theorem for cone-beam image reconstruction. J X-ray Sci Technol 2015;23(2):157–88.
[47] Iuso D, Paramonov P, De Beenhouwer J, Sijbers J. Practical multi-mesh registration for few-view poly-chromatic X-ray inspection. J Nondestruct Eval 2024;43(2):63.
[48] Yao W, Leszczynski KW. An analytical approach to estimating the first order X-ray scatter in heterogeneous medium. Med Phys 2009;36(7):3145–56.